
Hydrodynamic Simulations of Integrated Experiments Planned for the OMEGA/OMEGA EP Laser Systems

Introduction

The fast-ignitor concept^{1,2} separates the fuel assembly and fuel heating by using a laser pulse to compress the fuel to a high density and an ultrafast, high-intensity laser to heat the fuel. The ultrafast laser produces relativistic electrons with high efficiency (up to 50% has been reported³) that heat the fuel, significantly easing the requirements on the compression driver.^{2,4} Several options for the compression driver have been considered, including using a laser-heated or heavy-ion-beam-heated hohlraum or a direct-drive laser.

The Laboratory for Laser Energetics is building the OMEGA EP Laser System⁵ that will consist of two short-pulse (1 to 10 ps), high-intensity ($>10^{19}$ W/cm²) laser beams, each capable of delivering 2.6 kJ of energy to the 60-beam OMEGA⁶ target chamber. OMEGA EP is designed to act as a backlighter source for imploded high-areal-density cryogenic targets and as a tool to study high-intensity interaction physics and the transport of the relativistic electrons in imploded cryogenic targets. Integrated implosions on the combined OMEGA/OMEGA EP Laser Systems, starting in 2008, will validate the models used for the source and the transport of the relativistic electrons used in the simulation of hydrodynamic codes.

In this article, we present results of simulations of the interaction of relativistic electrons with cryogenic targets that are imploded with a pulse designed to achieve areal densities near 0.5 g/cm². The article is organized as follows: **Transport Model and Target Design** (p. 189) describes the models used in the source and transport of the relativistic electrons and the target and laser pulse designed to reach the required areal densities; **Simulation Results for Symmetric Implosions** (p. 191) presents the results of simulations carried out for uniform conditions; **Effect of Nonuniformity** (p. 193) describes the results for nonuniform implosions (power balance and ice roughness); and **Conclusions** (p. 194).

Transport Model and Target Design

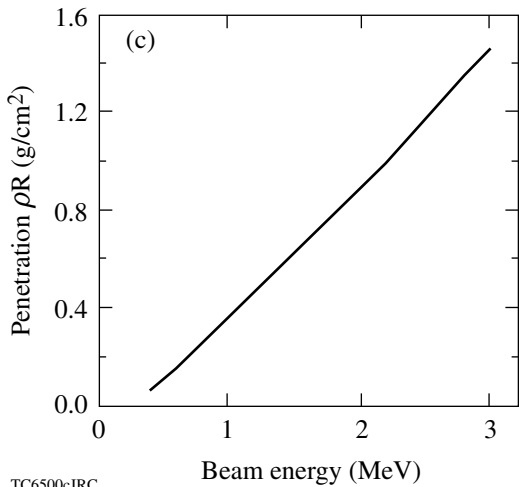
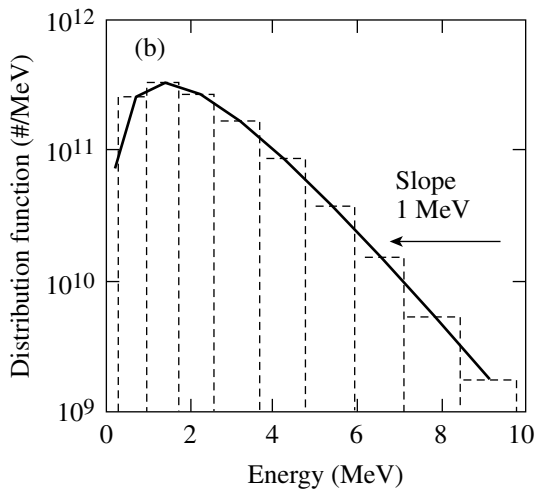
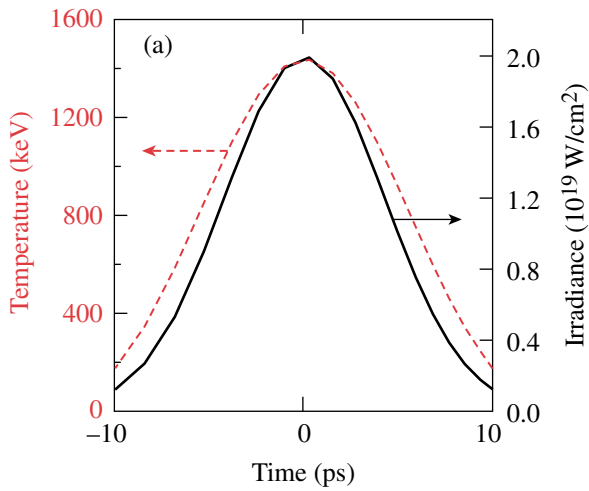
The simulation of the effects of the relativistic electron beam produced by the OMEGA EP laser requires the modeling of

the electron source and the transport of relativistic electrons in high-density materials. The characteristics of the electron source—the conversion efficiency, the spectrum (temperature) of the source, and the divergence of the electrons—are not well known because they are obtained from experiments and simulations that are carried out under conditions that are significantly different from those in an imploding target. Conditions at the end of a laser-produced channel or at the apex of a gold cone near the imploded core are that of a warm plasma (~200 eV) at near-solid density or slightly lower. Particle-in-cell (PIC) simulations are carried out for sharply rising pulses interacting with hot (several keV), low-*Z* targets.⁷ In experiments, short-pulse lasers ≤ 1 ps are focused on solid, mid-*Z* targets (usually Al) and the electron source characteristics are measured indirectly, mostly from K_{α} x-ray emission.⁸ For the simulations reported here, the source electrons are assumed to be Maxwellian with the semi-empirical temperature scaling given by⁷

$$T = 511 \times \left[\left(1 + I / 1.37 \times 10^{18} \right)^{0.5} - 1 \right] (\text{keV}), \quad (1)$$

where I is the laser intensity in W/cm². The electron source temperature, spectrum, and range are shown in Fig. 104.29 for a 2.5-kJ, 20- μ m-radius laser pulse. A Gaussian laser pulse is assumed with 10-ps full width at half maximum (FWHM). The peak laser intensity and source temperature are 2×10^{19} W/cm² and 1.4 MeV, respectively.

The physics of the transport of the electrons is very complex. PIC code and hybrid PIC code results show complicated magnetic and electric field structures near the electron source and filamentary structures that depend on the background electron density.⁹ A simple straight-line transport model has been chosen since such high-energy electrons are not scattered much in low-*Z* plasmas. In this model, the electrons lose energy because of collisions with thermal electrons and ions and to collective oscillations according to a formulation that takes into account multiple scattering.¹⁰ The model does not include electric or magnetic fields and Joule heating by the return current. Figure 104.29(c) shows the penetration depth as a function of electron energy in 300-g/cm³, 5-keV DT. A total areal density

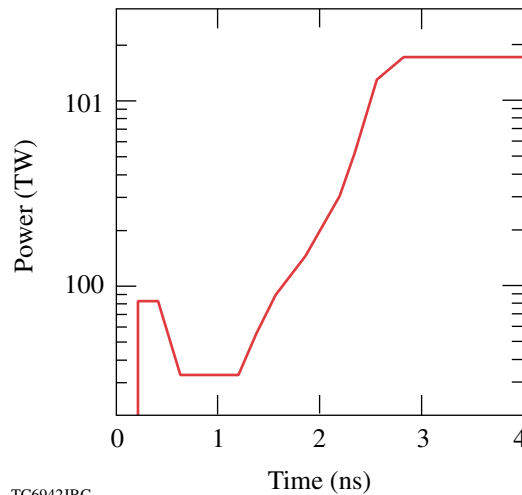
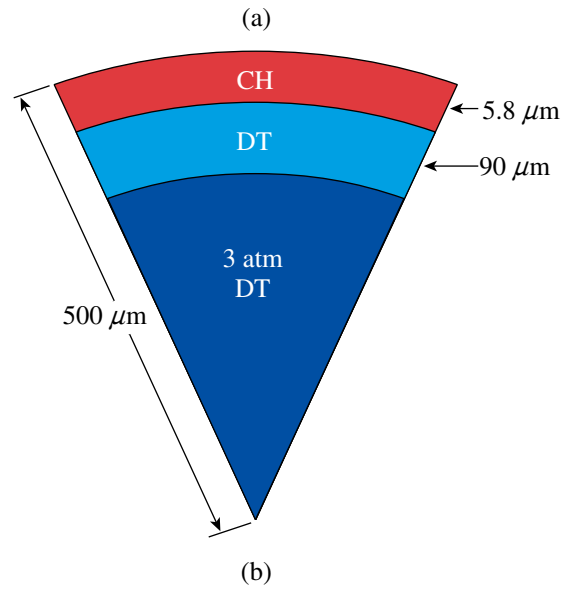


TC6500cJRC

Figure 104.29
 Details of the electron source: (a) temporal evolution of the laser intensity (dashed line) and source temperature (solid line) from Ref 7, (b) distribution function for a 1-MeV temperature and grouping, and (c) penetration depth of electrons in a 5-keV, 300-g/cm³ DT plasma.

of about 1 g/cm² is required to stop the 2-MeV electrons in the 1-MeV distribution in Fig. 104.29(b).

A cryogenic target has been designed to achieve the required core areal densities near 0.5 g/cm² that will stop electrons up to 2 MeV (total areal density of 1.0 g/cm² for a traversing electron). The target, shown in Fig. 104.30(a), is nearly identical to capsules currently being imploded on the OMEGA laser. The pulse shape in Fig. 104.30(b) was designed to provide 25 kJ at 351 nm while keeping the minimum isentrope during the



TC6942JRC

Figure 104.30
 Target design for uniform implosion: (a) target details and (b) shaped pulse producing $\alpha = P_e/P_{TF} < 2$. Nearly identical targets are being imploded on the OMEGA laser.

implosion to $\alpha = P_e/P_{TF} < 2$, where P_e is the electron pressure and P_{TF} is the Fermi pressure at $T_e = 0$. This isentrope is lower than that of present cryogenic implosions.¹¹ The maximum density and total areal density from a 1-D simulation with the hydrodynamic code *LILAC*¹² reach 500 g/cm^3 and 0.5 g/cm^2 , respectively. At peak areal density (3.96 ns) the residual gas inside the target is heated to several kilovolts, whereas the high-density shell is kept below 200 eV.

Simulation Results for Symmetric Implosions

Simulations to study the hydrodynamic response of the target to the energy deposited by the electrons were carried out for a uniform implosion with the 2-D hydrodynamic code *DRACO*.¹³ Uniform implosions can be simulated quickly and therefore permit the investigation of a larger parameter space than perturbed implosions. The electrons were produced at the pole as a cylindrical source directed parallel to the z -axis with radii varying from 5 to $30 \mu\text{m}$. The source was injected where the background electron density is $2 \times 10^{21} \text{ cm}^3$. The results are insensitive to the position of the source because the simulated electron beam has no divergence and the electrons are not effectively slowed until they reach much higher densities. The temporal Gaussian laser pulse produces 2.5 kJ of $1\text{-}\mu\text{m}$ light with the pulse duration varying from 1 to 30 ps FWHM. Two conversion efficiencies from the laser energy to the electron beam were assumed: 20% and 50%. The timing of the electron pulse with respect to the stagnation time was varied between -60 ps to 40 ps in intervals of 20 ps in order to study the sensitivity of the neutron yield to the timing.

The effect of the electron heating on the neutron production rate is illustrated in Fig. 104.31, where contours of neutron production rate per unit volume are shown at the time of peak neutron production. The mass density is shown in black contours. In Fig. 104.31(a), the neutron production in the case when the electron beam is not introduced is limited to the hot spot formed by the residual gas and a small layer inside the high-density shell. In Fig. 104.31(b), the neutron production extends over the path of the $20\text{-}\mu\text{m}$ -radius electron beam and has a greater spatial extent inside the shell than in Fig. 104.31(a). The peak neutron production occurs in a circular region in the hot core where a blast wave was created by the explosion of the shell from the heating by the relativistic electrons.

The temporal response of the stagnated core to the electron heating is shown in Fig. 104.32, where lineouts taken across the target $4 \mu\text{m}$ above the x axis in Fig. 104.31(b) of the neutron rate per volume, the ion temperature, and the mass density are plotted at four times with respect to the peak of the Gaussian high-intensity laser. The electron beam enters from the right. At the peak of the pulse [Fig. 104.32(a)], the shell has already been heated to about 2 keV as compared to the 200 eV shown in Fig. 104.30(c) without the heating beam. The shell starts to explode and decompresses and sends a blast wave into the core, which can be seen as a small jump in the ion temperature. Neutrons are produced in the high-density shell as well as in the core. The conditions in the shell are not uniform because more energy from the electron beam is deposited on the side nearer to the source (right-hand side) than on the far side. Since the

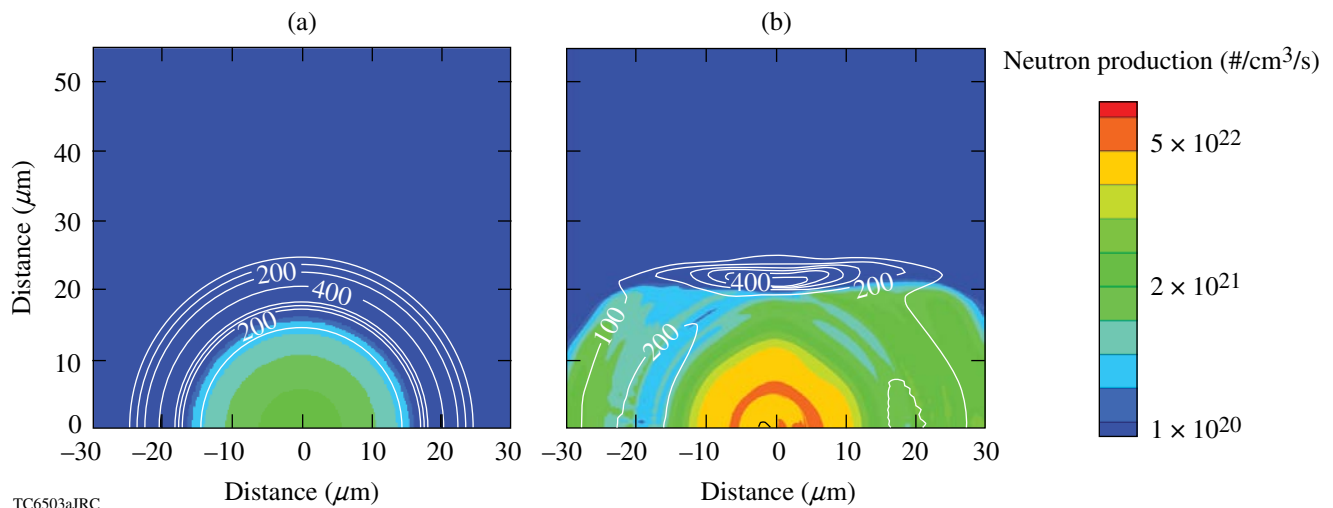
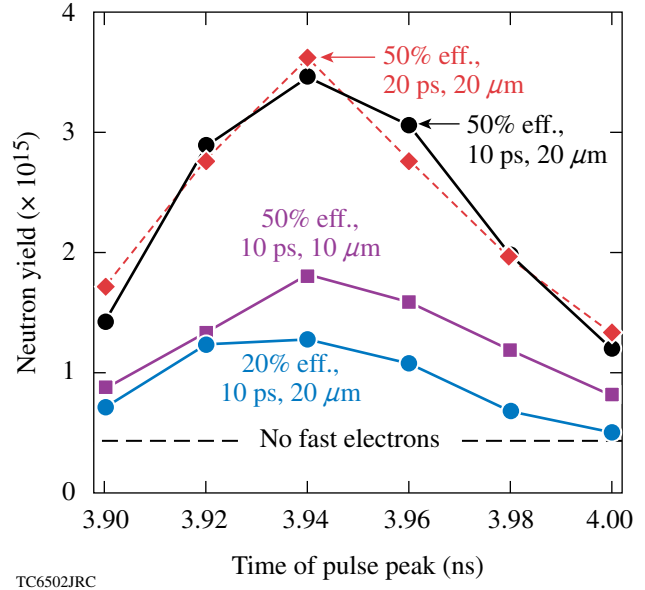


Figure 104.31

Contours of the neutron production rate per unit volume and mass density (black contours) at the time of peak neutron production in the case without an electron beam (3.95 ns) (a) and no electron beam. (b) 2.5-kJ, 50% conversion efficiency, 10-ps FWHM, and $20\text{-}\mu\text{m}$ -radius electron beam peaked at 3.94 ns.

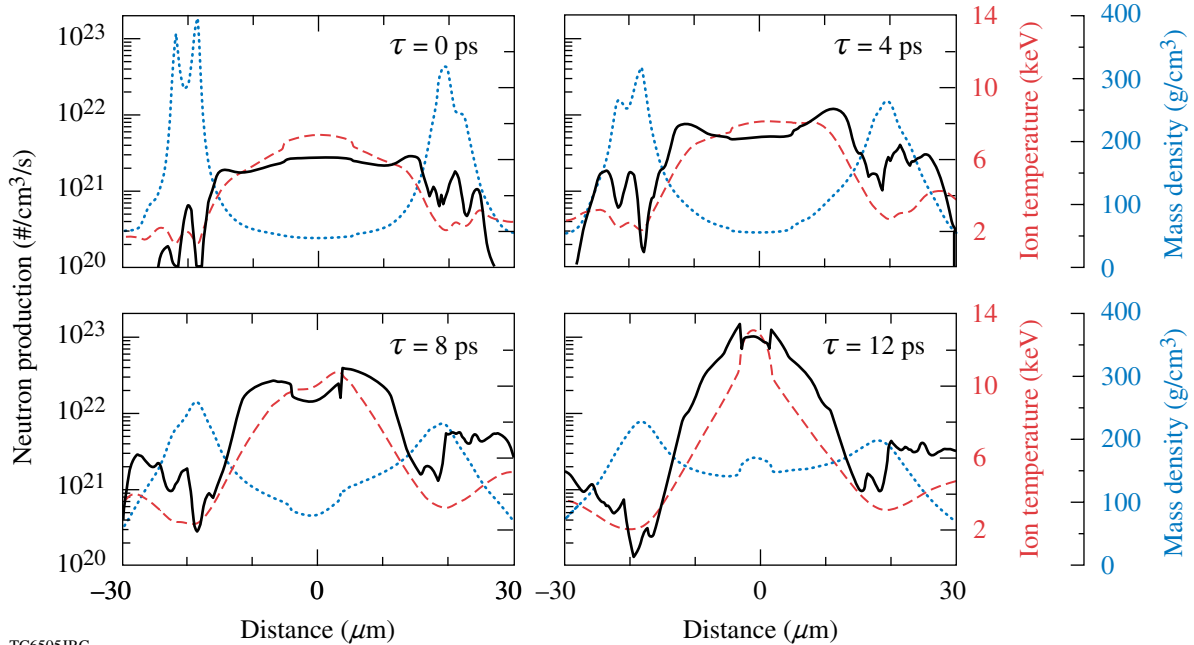
electrons are produced over a range of energies, the less-energetic electrons deposit most of their energy in the shell nearer the source, while the more-energetic electrons deposit their energy uniformly in both sides of the shell. In Fig. 104.32(b), 4 ps after the peak, the blast wave can be seen as small steps in both the ion temperature and the mass density. The neutron production rate is enhanced behind the blast wave. At 8 ps after the peak of the electron pulse [Fig. 104.32(c)], the shell density has decreased to about half its peak uniform value and the blast wave has almost reached the center of the core, heating it to about 10 keV. Neutrons are still being produced in the high-density shell where the ion temperature reaches almost 4 keV. In Fig. 104.32(d), 12 ps after the peak of the electron pulse, the blast wave has reflected from the target center, creating ion temperatures reaching 13 keV and a large neutron production rate, although the actual number of neutrons produced in that region is small because of its small volume. Large neutron rates still occur in the shell, though it is beginning to cool.

The sensitivity of the neutron yield to the timing of the high-intensity pulse for several laser conditions is shown in Fig. 104.33. In all cases, the peak yield occurs when the peak of the pulse is timed about 20 ps before peak stagnation (3.96 ps);



TC6502JRC

Figure 104.33
Sensitivity of the neutron yield to the laser pulse timing and characteristics. Peak areal density occurs at 3.96 ns.



TC6505JRC

Figure 104.32
Lineouts 4 μm above the x-axis of the neutron production rate (solid curve), the ion temperature (dashed curve) and the mass density (dotted curve); times are with respect to the peak of the 10-ps Gaussian electron pulse timed at 3.94 ns. The electron beam enters from the right.

the highest yield is about a factor of 8 higher than the yield from the implosion without electrons. The yield remains within a factor of 2 of the peak yield within a 100-ps range for the pulse timing. The 20-ps requirement on the timing specification for the OMEGA EP beams is well within this range. For the 50% conversion efficiency, the yields were the same for the 20-ps and the 10-ps beam FWHM and a 20- μm -beam radius. The higher source temperature from the shorter pulse's higher intensity is compensated by the deposition of more electron energy early in time before the shell has decompressed. Reducing the beam radius reduces the yield by about a factor of 2 because of two effects: the higher intensity leads to a higher source-electron temperature that produces more electrons that escape the core, and the beam only partially covers the core radius, heating less of the high-density shell. Reducing the efficiency to 20% reduces the neutron yield by about a factor of 3.

Effect of Nonuniformity

A series of simulations was carried out with the power-balance nonuniformity caused by the OMEGA 60-beam geometry; they also included alpha-particle transport during neutron production. A modified target design reached a slightly lower areal density than the previous one, 0.45 g/cm², and a lower peak density, 360 g/cm³, because the beam delivered 18 kJ instead of 25 kJ in the previous series of simulations. The high-intensity laser configuration and electron source are the same as in the previous series. Figure 104.34 shows the

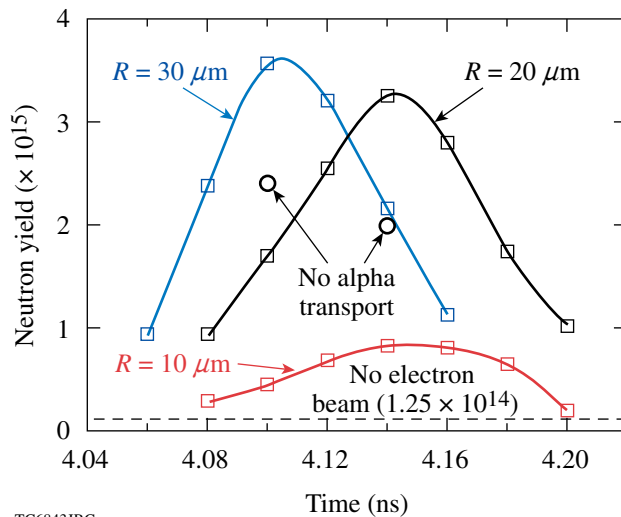


Figure 104.34 Sensitivity of the neutron yield to the laser pulse timing and characteristics for implosions that include the illumination nonuniformity due to OMEGA beam geometry. The pulse is 2.5 kJ, 10-ps FWHM with a 50% conversion efficiency. Open circles show the results of turning off the alpha transport.

sensitivity of the neutron yield on the timing of the ignitor pulse for three beam radii (10, 20, and 30 μm) from a 2.5-kJ, 10-ps FWHM laser with 50% conversion efficiency to electrons. The implosions without the electron beam produce a yield of 1.25×10^{14} . Introducing the electron beam increased the yield by about a factor of 25. A radius of 10 μm results in a lower yield because the laser intensity and the resulting electron source temperature are too high. The implosions with the larger electron-beam radii yield about the same maximum number of neutrons but at different beam timings. This is because the 30- μm beam produces a lower temperature electron source than that of the 20- μm beam, which is more efficient in heating the core uniformly earlier in time when the areal density of the shell is lower. The higher-temperature electrons from the 20- μm beam are more efficient later, near peak areal density. The timing sensitivity for producing more than half the peak yield is about 80 ps. The yields increased by about 50% when the alpha transport was included, showing the early phase of bootstrap heating.

Another series of simulations was carried out with the same target design and relativistic electron conditions as above but included two levels of inner-ice layer roughness, 2 and 4 μm σ_{rms} , which are larger than the expected values for these implosions.¹⁴ Figure 104.35(a) shows the perturbation cosine spectrum applied to the inner-ice surface with a random phase of $0, \pi$. The resultant core at the time of peak areal density (3.76 ns) in Fig. 104.35(b) shows nonuniform shell densities varying from 200 to 700 g/cm³. A 2.5 kJ, 10-ps FWHM laser pulse with a 20- μm radius was timed 40 ps before shell stagnation. The yields for the simulations with and without the electron beam are shown in Fig. 104.36(a) as a function of the inner-ice roughness σ_{rms} . As expected, the yield decreases in the absence of the electron beam because of the core distortions caused by the ice roughness,¹⁴ as shown in Fig. 104.35(b), down to about a factor of 6 from the uniform case at 4 μm of ice roughness. The neutron yield with the electron beam is almost a constant 10^{15} over the range of nonuniformity; in the case of 4 μm of ice roughness, the yield has improved by about a factor of 120 from that with no electron beams.

The neutron yield remains constant with increasing ice roughness when the electron beam is included because the radius of the high-density shell, whether distorted or not, is less than 20 μm [Fig. 104.35(b)], smaller than the 20- μm electron beam used in these simulations. Thus the electron beam heats the entire shell and raises the same amount of core material to the same temperatures in all cases of ice roughness, shown in Fig. 104.36(b). In the 4- μm - σ_{rms} case, the blast wave does not

converge uniformly as in the zero ice roughness case because of the nonuniform pressure in the distorted shell where it is generated. This leads to lower ion temperatures than in the uniform case, causing the small decrease in the yield observed in Fig. 104.36(a) for the electron beam case.

Conclusions

Two-dimensional hydrodynamic simulations were carried out to model the response of a cryogenic target imploded on the 60-beam OMEGA laser to the relativistic electron beam created by an OMEGA EP ultrafast laser beam. Targets were designed to produce areal densities near 0.5 g/cm^2 at stagna-

tion. A study with uniform implosion showed that the shell, heated by the electron beam, explodes and sends a blast wave into the low-density core. The neutron yield reached a factor of 8 higher than that of the case without the electron beam because of production in the heated ($\sim 2 \text{ keV}$) dense shell and increased

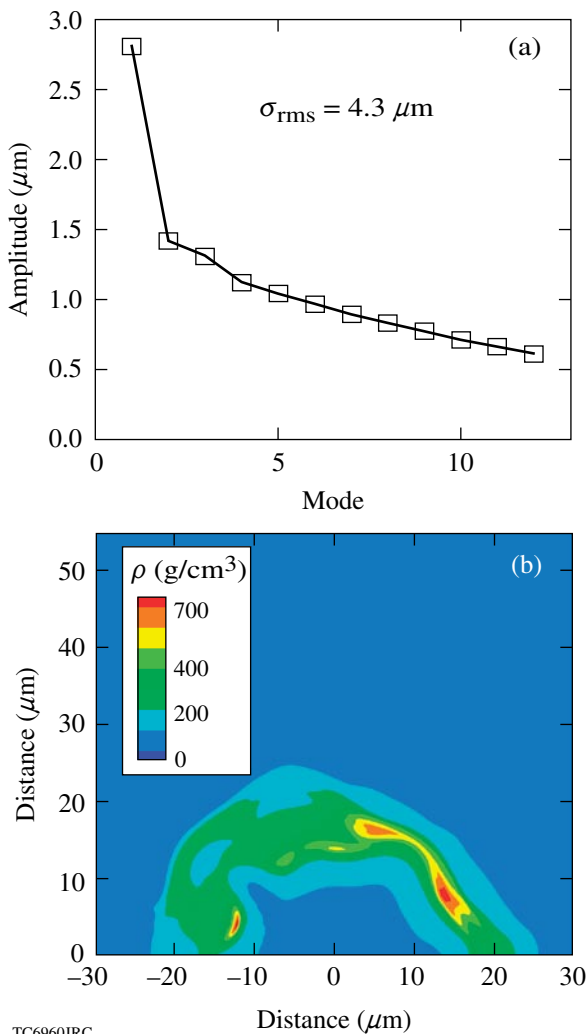


Figure 104.35 (a) Spectrum of the inner-ice roughness for $4\text{-}\mu\text{m}$ σ_{rms} and (b) core condition at stagnation.

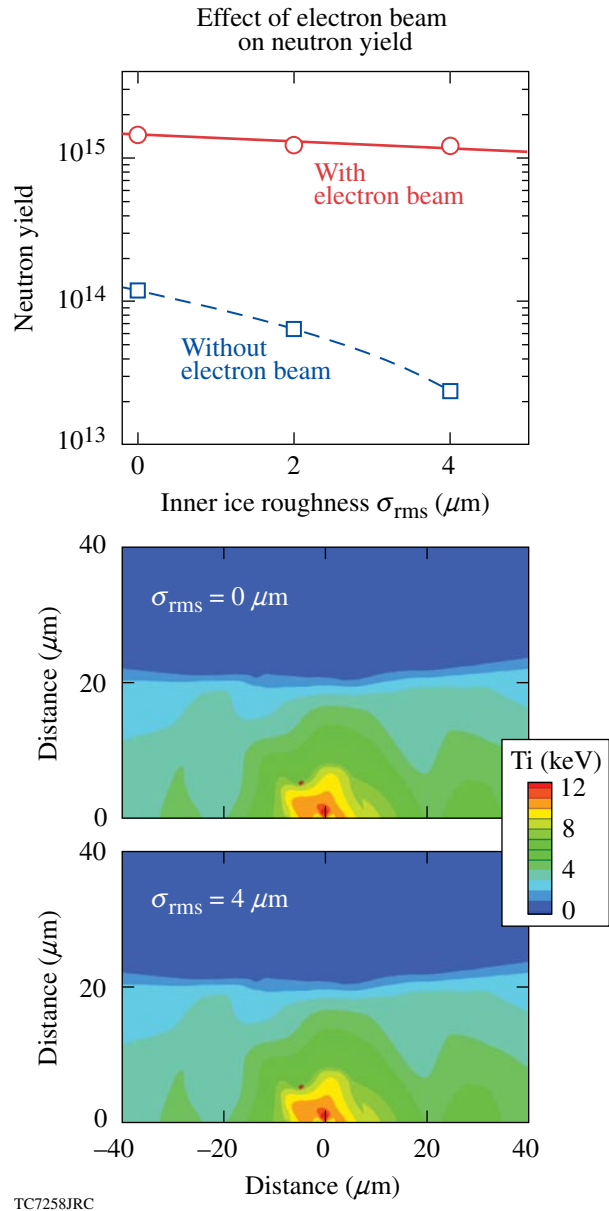


Figure 104.36 (a) Effect of the inner-ice roughness on the neutron yields—with the electron beam, the yield is constant for all levels of nonuniformity. (b) Ion temperature contours near time of peak neutron production for two ice roughness cases, $\sigma_{\text{rms}} = 0 \mu\text{m}$ and $4 \mu\text{m}$, showing that the same amount of shell material is heated by the $20\text{-}\mu\text{m}$ electron beam.

production in the low-density core heated by the blast wave. The highest yields—about 3.5×10^{15} and about a factor of 8 above the yield without the electron beam—were obtained for a 20- μm -radius beam with pulse durations of 10 and 20 ps timed 20 ps before stagnation. Yields within a factor of 2 of the peak yield were produced within a 100-ps timing window centered at stagnation. In a second study carried out with the illumination nonuniformity due to the OMEGA beam geometry, the highest yields (about 3.5×10^{15}) were produced at different beam timings for the 20- and 30- μm radii. These yields are about a factor of 25 larger than those without the electron beam. The inclusion of the alpha transport during neutron production increased the yield by about 50%. The final series of simulations were carried out with two levels of inner-ice nonuniformity, which produced a stagnating shell with nonuniform mass densities ranging from 200 to 700 g/cm^3 . A 10-ps FWHM, 20- μm -radius laser beam timed 40 ps before peak areal density increased the neutron yields by a factor of 120 from that without the electron beam for the largest level of ice roughness. The OMEGA EP beam is expected to produce neutron yields in excess of 10^{15} for all levels of inner-ice nonuniformity and to show the effects of bootstrap heating.

ACKNOWLEDGMENT

This work was supported by the U.S. Department of Energy Office of Inertial Confinement Fusion under Cooperative Agreement No. DE-FC52-92SF19460, the University of Rochester, and the New York State Energy Research and Development Authority. The support of DOE does not constitute an endorsement by DOE of the views expressed in this article.

REFERENCES

1. N. G. Basov, S. Yu. Gus'kov, and L. P. Feokistov, *J. Sov. Laser Res.* **13**, 396 (1992).
2. M. Tabak *et al.*, *Phys. Plasmas* **1**, 1626 (1994).
3. K. Yasuike *et al.*, *Rev. Sci. Instrum.* **72**, 1236 (2001).
4. S. Atzeni, *Phys. Plasmas* **6**, 3316 (1999).
5. J. D. Zuegel, S. Borneis, C. Barty, B. LeGarrec, C. Danson, N. Miyanaga, P. K. Rambo, T. J. Kessler, A. W. Schmid, L. J. Waxer, B. E. Kruschwitz, R. Jungquist, N. Blanchot, E. Moses, J. Britten, C. LeBlanc, F. Amiranoff, J. L. Porter, J. Schwarz, M. Geissel, I. C. Smith, I. Jovanovic, and J. Dawson, "Laser Challenges for Fast Ignition," submitted to *Fusion Science and Technology*; L. J. Waxer, D. N. Maywar, J. H. Kelly, T. J. Kessler, B. E. Kruschwitz, S. J. Loucks, R. L. McCrory, D. D. Meyerhofer, S. F. B. Morse, C. Stoeckl, and J. D. Zuegel, *Opt. Photonics News* **16**, 30 (2005).
6. T. R. Boehly, D. L. Brown, R. S. Craxton, R. L. Keck, J. P. Knauer, J. H. Kelly, T. J. Kessler, S. A. Kumpan, S. J. Loucks, S. A. Letzring, F. J. Marshall, R. L. McCrory, S. F. B. Morse, W. Seka, J. M. Soures, and C. P. Verdon, *Opt. Commun.* **133**, 495 (1997).
7. S. C. Wilks *et al.*, *Phys. Rev. Lett.* **69**, 1383 (1992).
8. K. B. Wharton *et al.*, *Phys. Rev. Lett.* **81**, 822 (1998).
9. L. Gremillet, G. Bonnaud, and F. Amiranoff, *Phys. Plasmas* **9**, 941 (2002).
10. C. K. Li and R. D. Petrasso, *Phys. Rev. E* **70**, 067401 (2004).
11. T. C. Sangster, J. A. Delettrez, R. Epstein, V. Yu. Glebov, V. N. Goncharov, D. R. Harding, J. P. Knauer, R. L. Keck, J. D. Kilkenny, S. J. Loucks, L. D. Lund, R. L. McCrory, P. W. McKenty, F. J. Marshall, D. D. Meyerhofer, S. F. B. Morse, S. P. Regan, P. B. Radha, S. Roberts, W. Seka, S. Skupsky, V. A. Smalyuk, C. Sorce, J. M. Soures, C. Stoeckl, K. Thorp, J. A. Frenje, C. K. Li, R. D. Petrasso, F. H. Séguin, K. A. Fletcher, S. Padalino, C. Freeman, N. Izumi, J. A. Koch, R. A. Lerche, M. J. Moran, T. W. Phillips, and G. J. Schmid, *Phys. Plasmas* **10**, 1937 (2003).
12. J. Delettrez, R. Epstein, M. C. Richardson, P. A. Jaanimagi, and B. L. Henke, *Phys. Rev. A* **36**, 3926 (1987).
13. P. B. Radha, T. J. B. Collins, J. A. Delettrez, Y. Elbaz, R. Epstein, V. Yu. Glebov, V. N. Goncharov, R. L. Keck, J. P. Knauer, J. A. Marozas, F. J. Marshall, R. L. McCrory, P. W. McKenty, D. D. Meyerhofer, S. P. Regan, T. C. Sangster, W. Seka, D. Shvarts, S. Skupsky, Y. Srebro, and C. Stoeckl, *Phys. Plasmas* **12**, 056307 (2005).
14. P. W. McKenty, V. N. Goncharov, R. P. J. Town, S. Skupsky, R. Betti, and R. L. McCrory, *Phys. Plasmas* **8**, 2315 (2001).